

Investigations of Aerodynamic Performance of Bell 412 Helicopter in Real-Time Hover Flight Conditions

H. Xu , S. Zhang , N. Ball and A. Gubbels

Institute for Aerospace Research (IAR)
National Research Council (NRC), Ottawa, Ontario, Canada
e-mail: Hongyi.Xu@nrc.ca

Key words: Rotorcraft Aerodynamics, Bell 412 Helicopter, Computational Fluid Dynamic (CFD) Simulation, Chimera Moving Grid Method

Abstract: The current research investigates the aerodynamic performance of a Bell 412 helicopter under both ideal-hover and real-hover flight conditions. A parametric study was conducted to investigate the aerodynamic performance of the isolated Bell 412 rotor in an ideal hover conditions. The in-flight measurements, conducted at the Flight Research Laboratory (FRL) of NRC-IAR, provided an invaluable database that permitted the study of a Bell 412 helicopter under real flight conditions. The real-time blade motion information was used as input to a CFD-FASTRAN flow solver, and the unsteady flow past Bell 412 helicopter was simulated based on the Euler equation model with the rotor-blades moving in a time-accurate manner. Pressure measurements on the fuselage from flight test were compared to the simulation results. Qualitative agreement was obtained in regions, such as the nose, cabin, etc. Discrepancies were found in regions, such as the vertical fin and tail rotor and engine inlet and exhaust areas. Explanations for the causes of these errors are provided. The current investigation predicted the rotor thrust and torque with a reasonable accuracy for the hovering condition, when compared with the flight test data. Flow visualization was used to present the prominent rotor downwash and the strong swirling flow field generated by the rotor blades. Aerodynamic performance of the rotor and the interaction with the fuselage were investigated by analyzing the pressure distributions and aerodynamic loads of both rotor blade and fuselage.

INTRODUCTION

Aerodynamics of rotary-wing flight vehicles involves a variety of complex flow phenomena, which present a grand challenge to the rotorcraft CFD community. These complex flows include: (1) transonic flow near the blade-tip, particularly on the advancing blade; (2) dynamic stalls on the retreating blade; (3) blade-tip vortices and their interactions; (4) strong flow interactions between the rotor and the fuselage. Since these flow phenomena govern the performance of a rotary-wing flight vehicle, it is crucially important to understand the physics behind these flows and to predict the phenomena based on an appropriate analytical model. So far, the advancement of computing technologies, both in numerical algorithms and computer architectures, has enabled the rotorcraft CFD community to successfully predict the attached subsonic/transonic rotor flows based on an Euler or Reynolds-Averaged Navier-Stokes (RANS) model [1]. A variety of other complex phenomena, most of them related to unsteady separations and turbulence, are yet to be satisfactorily resolved, and more advanced next-generation CFD models, such as Detached Eddy Simulation (DES) or Large Eddy Simulation (LES), are projected to play an important role in the future research activities.

Aside from modeling the complicated flow physics, the rotorcraft CFD community also has to face the unique challenge of grid generation in modeling rotorcraft flow. Due to the rotor blade rotation and the associated cyclic pitch, flap and lead-lag motions, a conventional multi-block grid with a fixed-grid topology would be difficult to be apply for meshing around the moving blades. In this regard, the Chimera moving grid technique, introduced by Steger et al. [2], provided the rotorcraft CFD community with an ability to generate well-formed grids capable of resolving the near-wall boundary layer of rotor blade without losing the flexibility of prescribing the complex blade motions. So far, this technique has been widely utilized in a variety of rotorcraft applications, which include multi-bladed rotors in hover and forward flight [3-7], and unsteady rotor-fuselage interaction [8].

In 2005, the rotary-wing program at the Aerodynamics Lab (AL) of NRC-IAR launched a Helicopter Modeling and Simulation project; one aim of which was to build an unsteady simulation capability of flows past a helicopter. The CFD-FASTRAN package from ESI was selected as the platform for development, which included the grid generator of CFD-GEOM, the flow solver of CFD-FASTRAN and the data post-processor CFD-VIEW. Since then, the Chimera moving grid capability in the package was comprehensively explored and carefully tested for a number of rotor configurations, including a two-bladed simple rotor in the forward flight conditions as reported in Xu et al. [9], a four-bladed rotor with cyclic pitching in Xu et al. [10] and the RoBin model helicopter in Xu et al [11]. These test cases were validated against a variety of benchmark data, including the experiments from Caradonna et al. [12], the measurements

from Elliott et al. [13] and the numerical results from Chen et al. [14] and Chaffin et al. [15]. These validations provided substantial confidence to push the flow simulation to more realistic helicopter configurations.

The current research investigates the aerodynamic performance of a Bell 412 helicopter under both ideal and real hover flight conditions. The flight measurements [16], performed at Flight Research Laboratory (FRL) of NRC-IAR prior to this investigation, provided an invaluable database that permitted validation of the CFD results from the current investigation. The measurement data included the pressure distributions on the Bell 412 fuselage surface and the real-time blade controlled motions of rotation, collective and cyclic pitching. The detailed collective and cyclic pitching motion schedules were determined by curve-fitting the measured data. The blade-motion information was used as input to the CFD-FASTRAN flow solver and the unsteady flow past the Bell 412 helicopter was simulated with the rotor-blades moving in a time-accurate manner. The pressure measurements on the fuselage were compared with the simulation results. A fairly accurate prediction of rotor thrust (within 7.5%) and torque or power consumption (within 26%) were obtained, comparing to the real-time flight data. The current paper will provide the details on the chimera grid generation strategy, the implementation of the blade motions and the investigations of Bell 412 helicopter aerodynamic performance through the CFD and experimental comparisons, the flow visualizations and the analyses of the simulated flow fields.

1. GOVERNING EQUATIONS AND NUMERICAL ALGORITHMS

The governing equations in CFD-FASTRAN [17] are derived by applying the conservations of mass and momentum to a control volume V with a boundary ∂V in a Cartesian coordinate system. The control volume moves and deforms at the volume surface velocity \vec{v}_g . The integral form of the governing equations can then be written as:

<p>(1) Continuity equation</p> $\frac{d}{dt} \iiint_V \rho dV + \iint_{\partial V} \rho (\vec{v} - \vec{v}_g) \cdot \vec{n} dA = 0 \quad (1.1)$	<p>(2) Momentum and energy equations</p> $\frac{d}{dt} \iiint_V \mathcal{Q} dV + \iint_{\partial V} (\vec{F}_c - \mathcal{Q} \vec{v}_g - \vec{F}_d) \cdot \vec{n} dA = \iiint_V \mathcal{S} dV \quad (1.2)$
---	---

where \mathcal{Q} is the conservative variables vector, $\mathcal{Q} = (\rho u, \rho v, \rho w, \rho E)^T$, \vec{F}_c is the convective (inviscid) flux and \vec{F}_d is the diffusive (viscous) flux, \vec{v}_g is the volume surface velocity and \mathcal{S} is the source term vector.

The flow is assumed to be inviscid in this investigation and the equations are reduced to Euler equations ($\vec{F}_d = 0$). This assumption significantly alleviates the grid density requirements near the walls, such as blade and fuselage surfaces and, therefore, greatly reduces the CPU time and memory requirements. Although the viscous effects are not included, the large-scale phenomena in helicopter flows, such as downwash, tip vortices and rotor-fuselage interactions, can still be, at least, qualitatively captured based on the current physical model.

The governing equations (1.1) and (1.2) are spatially discretized using the finite volume method. By applying the integral formulations of Eqs (1.1) and (1.2) to a finite control volume and using the divergence theorem, the following discretized form of the governing equations can be derived, where: \vec{n} is the cell face normal, subscription f denotes the surface indices of the control volume, ΔV and ΔA is the volume and the surface area of the control volume and δV is the volume change due to the grid motion. The \mathcal{Q} represents the conservative variables vector $\mathcal{Q} = (\rho, \rho u, \rho v, \rho w, \rho E)^T$; $\vec{F} = \vec{F}_c - \mathcal{Q} \vec{v}_g$ stands for the convective-moving flux and $\partial \vec{F} / \partial \mathcal{Q}$ and $\partial \mathcal{S} / \partial \mathcal{Q}$ are the flux Jacobian and source Jacobian, respectively.

$$\frac{\Delta \mathcal{Q}}{\Delta t} \Delta V^{n+1} + \sum_{f=1}^{N_f} \left[\frac{\partial \vec{F}_f}{\partial \mathcal{Q}} \Delta \mathcal{Q} \cdot \vec{n}_f^{n+1} \Delta A_f^{n+1} \right] - \left(\Delta V^{n+1} \frac{\partial \mathcal{S}}{\partial \mathcal{Q}} \right) \Delta \mathcal{Q} = \mathcal{S}^n \Delta V^{n+1} - \sum_{f=1}^{N_f} \vec{F}_f^n \cdot \vec{n}_f^{n+1} \Delta A_f^{n+1} + \mathcal{Q}^n \delta V \quad (1.3)$$

The flux vector and the flux Jacobians are evaluated using Roe's approximate Riemann solver, which is a flux difference scheme. High-order spatial accuracy is achieved using various gradient limiters. The Osher-Chakravarthy limiter is used in the current study to obtain a better flow quality since this limiter can produce a third-order accuracy.

2. GRID GENERATION and CHIMERA GRID

Figures 1(a) and (b) present the Chimera grid topologies for the isolated Bell 412 four-bladed rotor and the Bell 412 helicopter with the four-bladed main rotor at zero degree blade rotational angle ($\psi = 0^\circ$ where ψ is the angle between the rotor blade and the x -axis positive downstream). For the isolated rotor case, as seen in Figure 1(a), the C-H grid around each of the four rotor-blades was structured with two-blocks that were imbedded in the background cylindrical

grid. The grid size was at $I \times J \times K = 67 \times 20 \times 44$ for each block with a total of 59 mesh points that were distributed along the profile of the blades in the chord-wise direction. The background grid contained two half cylindrical domains, with the diameter of the domain at $25m$ and the height of the domain at $20m$. 50 points were used in the radial direction, 60 points in the circumferential direction and 59 points in the height direction. For the Bell 412 helicopter configuration in Figure 1(b), the background grid was build around the Bell 412 fuselage, which contained 12 multi-block structures with a C-gridding strategy used in the streamwise direction and an O-gridding strategy applied in the circumferential direction. The total number of grid points was about 1.82 million unevenly distributed within the 12 blocks. The rotor blades were meshed based on a topology and grid-size the same as the isolated rotor. All these meshes were generated by CFD-GEOM [17] based on the CAD geometries of Bell 412 rotor-blades and fuselage.

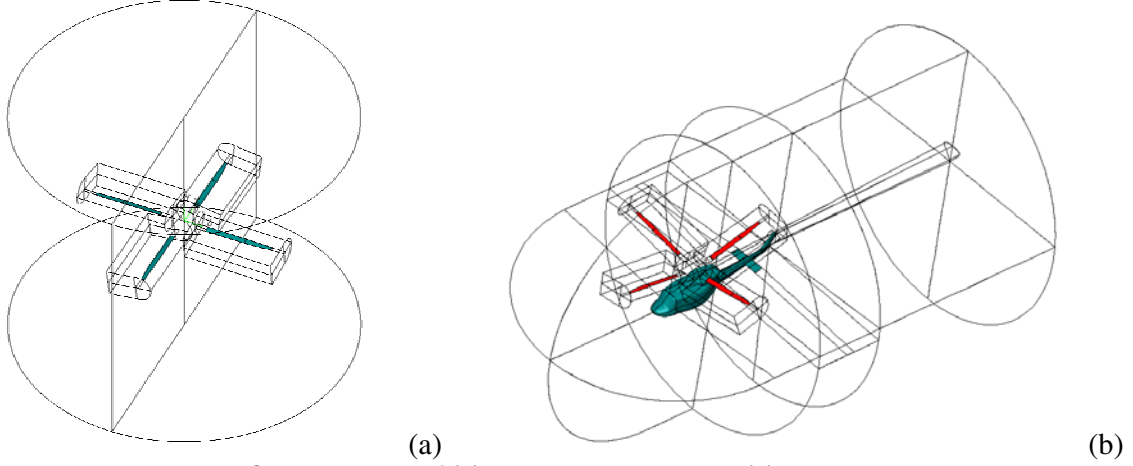


Figure 1: Grid topologies of (a) Bell 412 isolated rotor; (b) Bell 412 helicopter

3. ROTOR BLADE MOTION

As demonstrated in Figure 2, the blade cross-section has a non-uniform profile and is twisted in the span-wise direction, with the blade chord being tapered near the tip. In the current investigation, the controlled blade motions, including the rotation and the collective and cyclic-pitching motions, were obtained from the recorded in the flight data as described in [16] and these motions were prescribed by assigning the corresponding grid velocity to the Chimera blade-domain (see reference [16] for more details). The averaged flapping effects were implemented by prescribing a coning angle and the flap fluctuation was ignored in the current hover case although the CFD-FASTRAN solver has the capability to prescribe these motions through its motion-module. The flapping fluctuation will be included in the future work, particularly for the forward flight in which the flapping motion plays an important role.

According to Gubbels et al. [16], the rotor has a radius of $R = 7.00m$ and rotates at $\Omega = 324rpm$, which gives a tip Mach number approximately 0.68. The implementation of rotation motion is straightforward. However, the collective and cyclic pitch information has to be obtained from the relationship of the cyclic control position to the rotor-blade pitch angle.

As illustrated in Figures 3 and 4(a), for the Bell 412 helicopter, the limiting cyclic-control positions include: (1) longitudinal stick positions at $6.0in$ of forward-stop and $-6.0in$ of aft-stop; (2) lateral stick positions at $6.0in$ of starboard-stop and $-6.0in$ of port-stop; (3) collective stick positions at $(y_{co})_{dn} = 0.0in$ of down-stop and $(y_{co})_{up} = 10.7in$ of up-stop. Gubbels et al. [16] provides the longitudinal cyclic and lateral cyclic calibrations, in which the blade pitch angle θ is linearly linked with the control stick position y through the following relations of $\theta_{lg,r} = c_0 + c_1 y_{lg,r}$ and $\theta_{lar} = d_0 + d_1 y_{lar}$ for longitudinal and lateral cyclic, respectively.

The calibrations of these coefficients, at their corresponding limiting stops (port and starboard for lateral, forward and aft for longitudinal), were given by the flight test data [16] at the five azimuth angles of 103° , 148° , 193° , 238° and 283° degrees. The coefficients in between the relevant stops are assumed to have linear change with the corresponding stick position, i.e. $c_0 = a_1 + a_2 y_{lar}$; $c_1 = a_3 + a_4 y_{lar}$ and $d_0 = b_1 + b_2 y_{lg,r}$; $d_1 = b_3 + b_4 y_{lg,r}$. Therefore, with the c_0 , c_1 values in Table 2 and d_0 , d_1 values in Table 3 of [16] and the limiting longitudinal and lateral stick positions given

above, the a_1, a_2, a_3, a_4 and b_1, b_2, b_3, b_4 can be calibrated at the above five azimuth angles for the up and down collective stick positions. Again, the blade pitch angles in between the up and down collective positions are assumed to have a linear variation that gives this formulation to calculate the blade pitch angles: $\theta = \theta_{dw} + (\theta_{up} - \theta_{dw}) / [(y_{co})_{up} - (y_{co})_{dw}] \times [y_{co} - (y_{co})_{dw}]$. The blade pitch angles obtained from the longitudinal and lateral calibrations are then averaged, which generates the blade motion information for aerodynamic simulation.

In current study, the hover flight cases, A054409-R16(hover), is selected for investigation. By applying the recorded data [16] of longitudinal, lateral and collective control positions to the formulations mentioned above, the blade motion information was retrieved at the five azimuth angles of $103^\circ, 148^\circ, 193^\circ, 238^\circ$ and 283° . As seen in Figure 4(b), the curve-fitting method was then applied to the five discrete blade pitch angles for the hover flight case, resulting in the following detailed blade motion schedule for one rotation: A054409-R16 (hover flight): $\theta = 7.43 - 6.16 \sin(\omega t)$

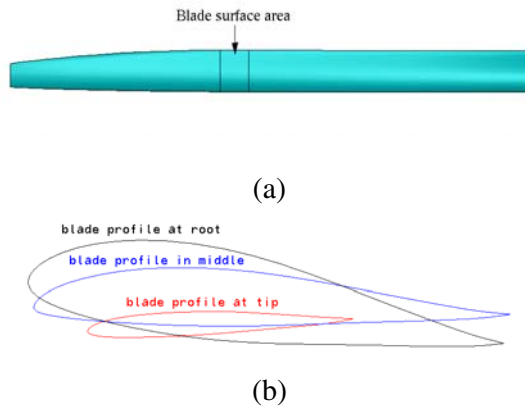


Figure 2: (a) Blade geometry; (b) Section profiles

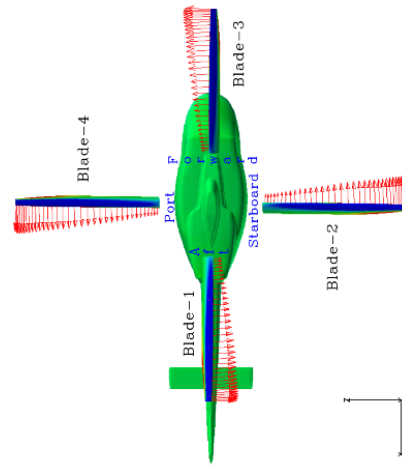


Figure 3: Longitudinal and lateral stick positions

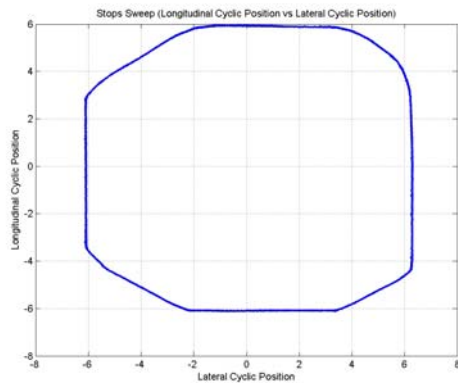


Figure 4(a): Sweep of the cyclic at the stops

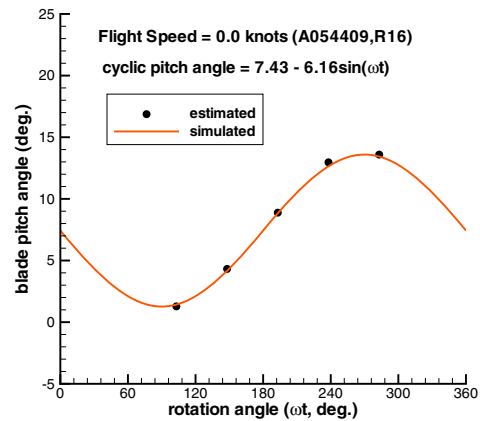


Figure 4(b): Blade pitching schedules for hover flight

4. PRESENTATION AND DISCUSSION OF RESULTS

4.1 Performance of Bell 412 isolated Rotor in Hover

Since the rotor aerodynamics dominates the flow past a helicopter, it was important, as a first step, to study the performance of the isolated rotor. This was helpful towards understanding the flow past the real helicopter (rotor and fuselage). The isolated rotor was studied under the ideal hover flight condition, which included: (1) demonstration of hover flow field of the four-blade isolated rotor; (2) investigation of load distributions on the rotor rotating plane and (3) parametric study of rotor performance at a variety of collective pitch angles.

Figures 5 (a) and (b) provide the flow visualizations of the isolated rotor, presented by the streamline particles, in the hover flight condition with each of the blade operating at six degrees of collective pitch angle. The blade surfaces are colored by the pressure magnitude. The streamline particles in Figures 5(a) and (b) are colored using different pressure ranges to show the general pattern of the pressure field and its relation to the flow field. Figure 5(a) presents the prominent feature of downwash with the fluid being pushed down by the rotor blade in a swirling manner. The rotation of the blades generates the low-pressure regions on top of the blade surfaces, as seen by the color of the fluid particle traces immediately above the blade. Figure 5(b) clearly presents the blade-tip vortex path that is featured by a relatively lower pressure above the rotor plane and a higher pressure region underneath the rotor plane.

The load and torque intensity distributions in the rotor rotating plane, including the out-plane load intensity F_y and torque intensity M_y and the in-plane load intensities F_x , F_z and torque intensities M_x , M_z , are provided in Figures 6 (a), (b) and (c). Here the load and torque intensities are defined as the force and moment divided by their corresponding blade surface area in Figure 2(a). In Figure 6 (d), F_x and F_z were converted to the in-plane load intensity of F_r (the load intensity in the radial direction, positive pointing away from rotation center) and F_t (the load intensity perpendicular to the radius). The torque was calculated with the reference point at the center of the rotation. As expected, the out-plane load and torque intensities are symmetric with respect to rotating axis (y -axis) and uniform in the azimuth direction. The radial distributions of F_y and M_y are presented in Figures 7(a) and (b). Figure 7(a) indicates that the rotor load intensity increases from the root to the near-tip region and then decreases because of the effects of blade-tip vortices. The curve has an inflexion point at about 75-80% of the rotor radius, primarily due to the combined effects of the design convention that a blade profile usually carries a zero twist at 75% of the rotor radius (see Leishman [18]) and the tip vortex influence as seen in Figure 5(b). The torque intensity in Figure 7(b) indicates that the rotor power consumption monotonously increases from the root to the tip. Although the load capacity drops near the tip due to the effects of blade tip vortices, the power consumption intensity increases sharply in this region, causing a high energy-loss and power inefficiency. The symmetric distributions of (F_x, F_z) and (M_x, M_z) , as seen in Figures 6 (b) and (c), indicate that the loads and torques are balanced in the rotor rotating plane. It is interesting to note that an evident phase-lag of (F_x, F_z) can be observed in Figure 6(b). For example, the maximum F_x is expected to occur at the position of 90° rotation angle (indicated by the red line), however, the actual maximum F_x occurs at about 70° after the red line and the same phenomenon also applies for F_z . For (M_x, M_z) , no phase-lags are observed as presented by Figure 6(c). Obviously, the phase changes were due to the strong swirling effects, as seen in Figure 5(b), which significantly deflect the local incoming flow angle for the rotor blades. The symmetrical distribution of F_t with respect to the rotation center in Figure 6(d) provides a verification of the distribution of M_y in Figure 6(a), since M_y was generated by F_t . The radial in-plane load intensity F_r in Figure 6(d) indicates that the rotor blade subjected to an aerodynamic load pointing towards the rotation center, which could offset some of the centrifugal load of the blade due to the rotation.

The parametric study of the isolated rotor in hover, as presented in Figure 8, gives the variation of thrust and torque (or power consumption) coefficients with the blade collective pitch angles. The load increases linearly with the collective pitch in the range from 4° to 16° , whereas the power consumption increases in a quadratic fashion with the collective pitch. The coefficients are obtained by the characteristic load and torque based on the tip velocity.

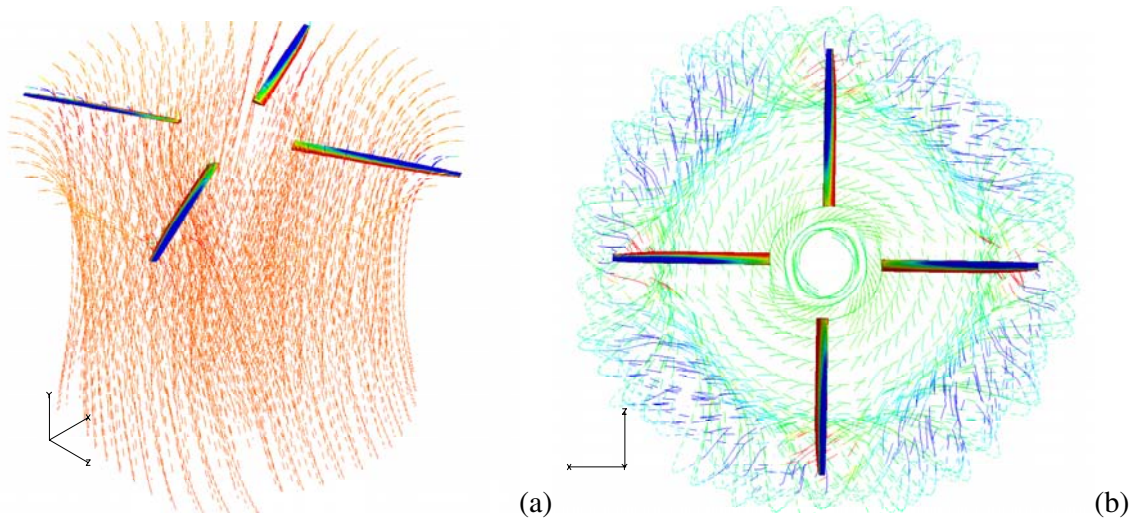
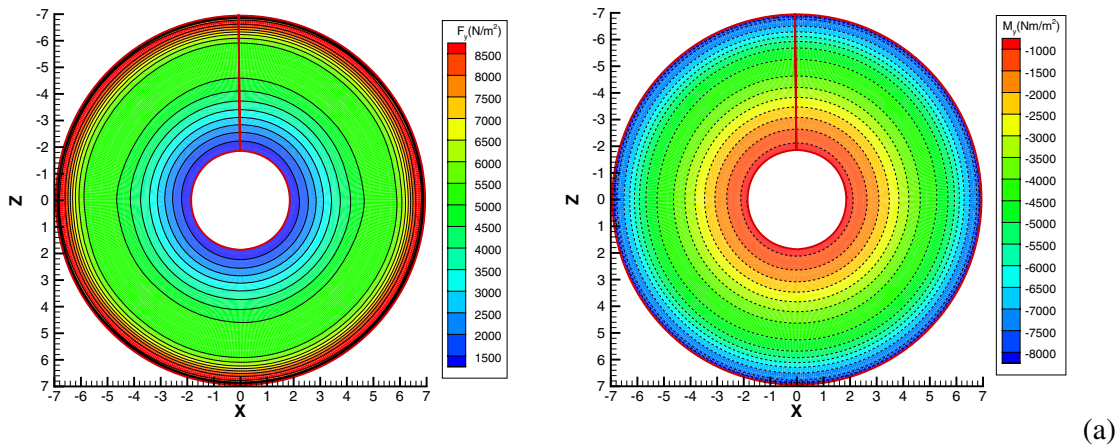
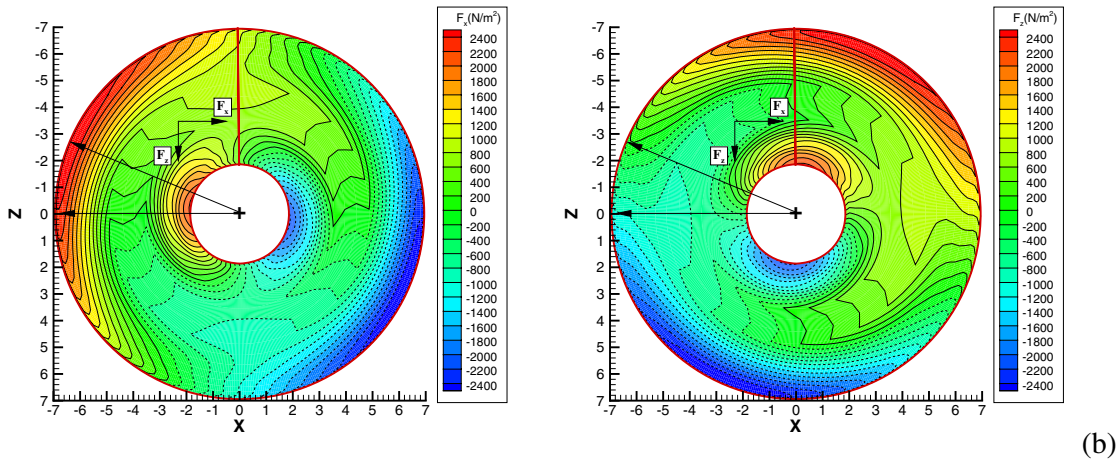


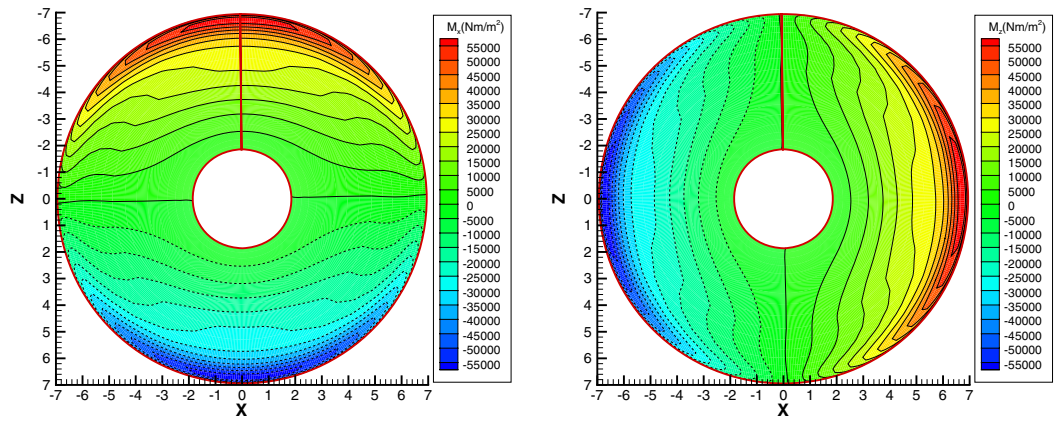
Figure 5: Isolated rotor flow field in hover (a) iso-angle view; (b) topview



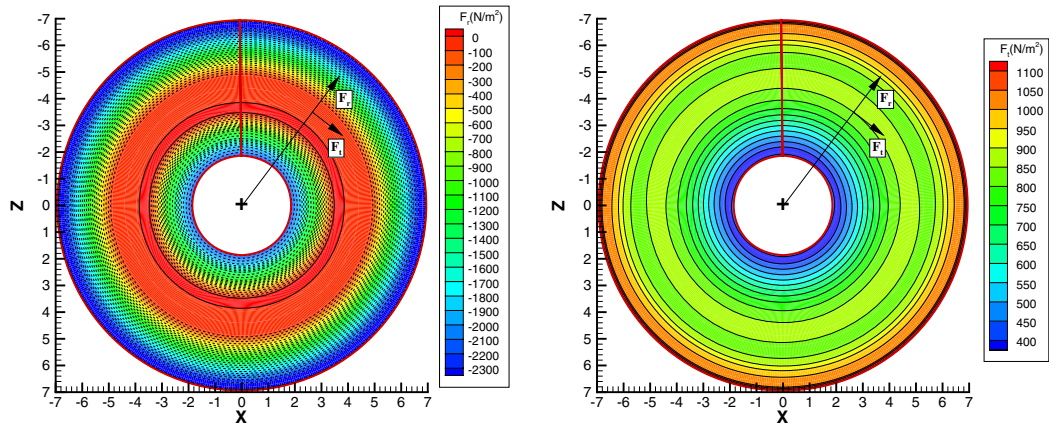
(a)



(b)

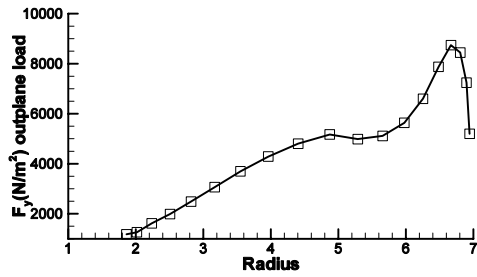


(c)

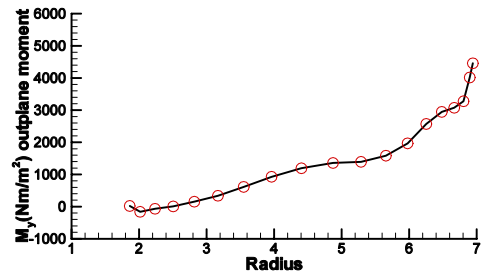


(d)

Figure 6: Isolated rotor load and torque intensity distributions (a) F_y and M_y ; (b) F_x and F_z ; (c) M_x and M_z ; (d) F_r and F_t .



(a)



(b)

Figure 7: Isolated rotor out-plane (a) load intensity and (b) torque intensity distributions in radial direction